FlexScale: Modeling and Characterization of Flexible Scaled Sheets

JUAN MONTES MAESTRE*, ETH Zürich, Switzerland
YINWEI DU*, ETH Zürich, Switzerland
RONAN HINCHET, ETH Zürich, Switzerland
STELIAN COROS, ETH Zürich, Switzerland
BERNHARD THOMASZEWSKI, ETH Zürich, Switzerland

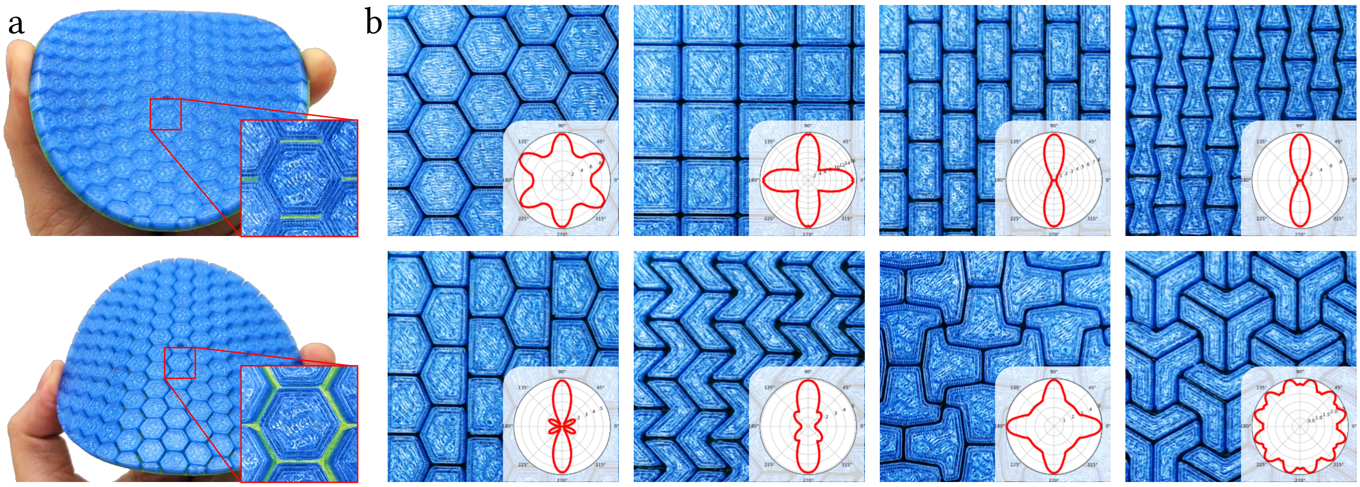

Fig. 1. Flexible scaled sheets offer a unique and intriguing combination of strength and flexibility. *a*: Bending-induced contact between scales leads to distinct behavior for positive (*top*) and negative (*bottom*) curvatures. *b*: our homogenization approach enables us to capture the macro-mechanical curvature response of arbitrary scale patterns.

We present a computational approach for modeling the mechanical behavior of flexible scaled sheet materials—3D-printed hard scales embedded in a soft substrate. Balancing strength and flexibility, these structured materials find applications in protective gear, soft robotics, and 3D-printed fashion. To unlock their full potential, however, we must unravel the complex relation between scale pattern and mechanical properties. To address this problem, we propose a contact-aware homogenization approach that distills native-level simulation data into a novel macromechanical model. This macro-model combines piecewise-quadratic uniaxial fits with polar interpolation using circular harmonics, allowing for efficient simulation of large-scale patterns. We apply our approach to explore the space of isohedral scale patterns, revealing a diverse range of anisotropic and nonlinear material behaviors. Through an extensive set of experiments, we show that our models reproduce various scale-level effects while offering good qualitative agreement with physical prototypes on the macro-level.

CCS Concepts: • **Computing methodologies** → **Modeling and simulation**; • **Applied computing** → *Computer-aided design.*

Additional Key Words and Phrases: Homogenization, Mechanical Characterization, Bi-Phasic Materials, Data-Driven Macromechanical Model

ACM Reference Format:
Juan Montes Maestre, Yinwei Du, Ronan Hinchet, Stelian Coros, and Bernhard Thomaszewski. 2024. FlexScale: Modeling and Characterization of Flexible Scaled Sheets. *ACM Trans. Graph.* 43, 4, Article 86 (July 2024), 14 pages. https://doi.org/10.1145/3658175

*Both authors contributed equally.

Authors' addresses: Juan Montes Maestre, ETH Zürich, Switzerland, jmontes@inf.ethz.ch; Yinwei Du, ETH Zürich, Switzerland, yinwei.du@inf.ethz.ch; Ronan Hinchet, ETH Zürich, Switzerland, ronanhinchet@gmail.com; Stelian Coros, ETH Zürich, Switzerland, stelian@inf.ethz.ch; Bernhard Thomaszewski, ETH Zürich, Switzerland, bthomasz@ethz.ch.

0730-0301/2024/7-ART86 $15.00
https://doi.org/10.1145/3658175

1 INTRODUCTION

Dense arrays of rigid scales embedded in soft skin protect animals from predator teeth. From turtles to turbots and from aligators to armadillos—scale shape, size, and arrangement combine to provide an ideal balance between rigidity and flexibility. Scaled animal skins have inspired manifold applications, including protective gear, skins for soft robots, and 3D-printed fashion. To unlock the full potential of synthetic scaled materials , however, we must understand how scale shape and arrangement mediate macro-mechanical behavior.

In this work, we systematically explore the mechanical behavior of scaled sheet materials—3D-printed hard scales embedded in a soft substrate. We focus on scale patterns defined through isohedral tilings [Kaplan and Salesin 2000; Schumacher et al. 2018], giving rise to a large and diverse space of patterns. The curvature response of these patterns is highly complex: the bi-material distribution induced by the scale pattern leads to large directional variations in bending stiffness; larger curvatures induce contact between scales, which rapidly increases stiffness; and structural asymmetry through the thickness leads to distinct bending responses for positive and negative curvatures. Each of these effects depends in nontrivial ways on scale shape and arrangement, making it challenging to predict the mechanical properties of a given pattern.

To address this problem, we propose a computational approach for modeling the mechanical behavior of scaled sheet materials. The basis for our method is formed by an accurate native-scale simulation model that combines soft shell elements with hard volumetric scales and penalty-based contact. To probe the mechanical behavior of arbitrary patterns in simulation, we develop a uni-axial bending test with tailored periodic boundary conditions that generate desired curvatures without hampering in-plane deformations. We use the data obtained from these experiments to construct a novel homogenized energy model that combines piecewise-quadratic uniaxial fits with polar interpolation based on circular harmonics. We further demonstrate that this homogenized energy can be combined with standard shell models to enable efficient simulation of large-scale patterns.

To validate our simulation models, we perform an extensive experimental analysis. In particular, we verify that scale-level effects are faithfully reproduced by our native-scale model. We further measure the macro-level bending resistance of 3D-printed prototypes using a dedicated testing device. The results indicate good qualitative agreement between simulations and measurements.

2 RELATED WORK

Metamaterial Design. Through precisely architected microstructures, flexible metamaterials can achieve a broad range of macromechanical properties [Bertoldi et al. 2017]. Fueled by the increasing availability of 3D printing technology, the graphics community has started to embrace the problem of generating 3D-printable content such as models optimized for stability [Lu et al. 2014; Stava et al. 2012; Zhou et al. 2013], mechanical assemblies [Ceylan et al. 2013; Coros et al. 2013; Thomaszewski et al. 2014; Zhu et al. 2012], or characters that can be posed and deformed in desired ways [Bächer et al. 2012; Skouras et al. 2013]. One particular line of research in this context investigates the creation of 3D-printable metamaterials. The spectrum includes layered materials fabricated with multi-material printers [Bickel et al. 2010], materials with lattice- [Panetta et al. 2017, 2015], voxel- [Schumacher et al. 2015; Zhu et al. 2017], and foam-like [Martínez et al. 2016, 2017] structures, as well as (extruded) planar microstructures [Li et al. 2023; Tozoni et al. 2020; Zhang et al. 2023] and sheet-like materials [Leimer and Musialski 2020; Martínez et al. 2019; Montes et al. 2023; Schumacher et al. 2018] . While these previous works have explored many aspects of mechanical metamaterials, they all focus on elastic behavior. In contrast, we investigate a new class of metamaterials whose macro-scale behavior is regulated by internal contact, not elastic deformation.

Interlocking Materials & Structures. Using interlocking as a mechanism for creating stable assemblies is a concept that is used across architecture, robotics, and material sciences. For example, interlocking can be used to build functional furniture without nails or adhesives [Song et al. 2017; Yao et al. 2017], rigid assembly puzzles [Song et al. 2012; Wang et al. 2018; Xin et al. 2011], and stable surfaces made from flexible [Skouras et al. 2015] or rigid [Wang et al. 2019] components. Depending on their shape, scales can likewise show interlocking behavior, leading to complex coupling even for *opening* curvatures. Even without an elastic medium, rigid elements can still provide meaningful flexibility [Lensgraf et al. 2020]. In this context, Tang et al. [2023] describe a framework for computational modeling and mechanical characterization of materials made from discrete interlocking elements. The macromechanical behavior of these generalized chainmail materials is governed by anisotropic deformation limits that arise due to contact between elements. The materials that we study in this work are dominated by internal contacts, but whereas discrete interlocking elements are purely kinematic, our method accounts for the complex coupling between quasi-rigid scales and the soft substrate in which they are embedded. A material system similar to ours was employed by Guseinov et al. [2017], who embed rigid prism elements with tailored geometry in pre-stretched membranes. Whereas their goal is to achieve desired deployed states upon release, we investigate the macro-mechanical properties of scaled sheets.

Homogenization. Homogenization provides a mathematical toolset for characterizing the macromechanical properties of metamaterials of structured materials [Bensoussan et al. 1978]. Most approaches use the same discretization (e.g., solid finite elements) for both native- and macro-level simulation [Kharevych et al. 2009; Panetta et al. 2015; Schumacher et al. 2015]. However, there are also methods that map between different computational models, for example from elastic rods to thin plates [Schumacher et al. 2018] or thin shells [Sperl et al. 2020], and from volumetric solids to rods [Rodriguez et al. 2022] . Our method is likewise a cross-discretization approach, but we map from a bi-material simulation with mixed solid and shell elements to a pure thin shell model.

Scaled Materials. The mechanics of natural dermal armor have been studied intensively using both experimental [Chen et al. 2011; Martini et al. 2017; Rudykh et al. 2015; Yang et al. 2013] and computational [Shafiei et al. 2021; Vernerey et al. 2014] methods. Closest to our work, Shafiei et al. [2022] study the mechanics of scale patterns using a discrete element approach. While their focus is primarily on puncture resistance, we characterize the anisotropic, nonlinear bending stiffness induced by inter-scale contact. We furthermore condense native-scale simulation data into a macro-mechanical that enables rapid simulation of large-scale patterns.

3 COMPUTATIONAL MODELING OF SCALED SHEETS

Flexible scaled sheets exhibit complex mechanical behavior that we aim to capture with our computational model. The bi-material distribution induces anisotropy in bending even for small deformations. Contact between scales leads to nonlinear stiffening. This effect is typically more pronounced in the closing direction of the scales, but can also occur for in the opposite, opening direction for non-convex scale shapes. Finally, while scaled sheets are flexible and readily

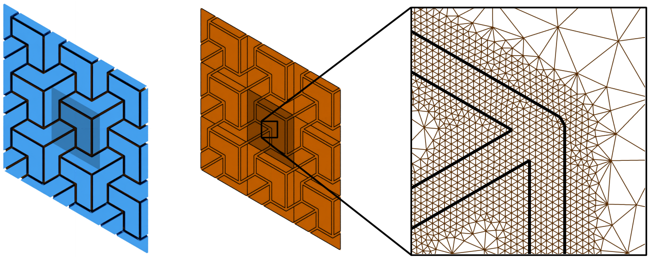

Fig. 2. Scale (*left*) and substrate (*middle*) meshes are generated from isohedral tilings. To facilitate coupling, the substrate is meshed such as to conform to the boundaries of the scale mesh (*right*).

permit uniaxial bending, they strongly resist bi-axial curvature. This is explained by the fact that Gaussian curvature entails stretching of the substrate, which—due to the stiff in-plane response of our scaled sheets—is energetically prohibitive. We therefore focus on characterizing the macro-mechanical bending response using dedicated uniaxial bending tests (Sec. 3.2). The data obtained with these simulation experiments is then used to construct a macro-mechanical model (Sec. 3.3). We start by describing our native-scale simulation model.

3.1 Native-Scale Simulation

Since scales will not deform noticeably during bending, we use a coarse discretization with linear tetrahedron elements. To model the compliant substrate we use discrete shell elements based on per-triangle shape operators [Gingold et al. 2004; Grinspun et al. 2006] combined with constant strain triangles for in-plane deformations. We use a Neo-Hookean constitutive model for both substrate and scale elements with material parameters chosen according to manufacturer specifications (see Sec. 4).

Substrate-Scale Coupling. Substrate and scale meshes must be coupled for simulation. To this end, we first generate a triangle mesh for the substrate that conforms to the scale boundaries; see Fig. 2 for an illustration. Substrate nodes below scales are then eliminated from the degrees of freedom and replaced by barycentric coordinates to implement kinematic coupling. We denote the remaining degrees of freedom as $\mathbf{x}$ and refer to substrate and scale elastic energies as $W_{\text{substrate}}$ and W_{scales}, respectively.

3.2 Homogenization

Parameterization. We probe the mechanical behavior of scaled sheets using native-scale simulation with uniaxial bending conditions. To impose these deformations on a unit cell, we start with a standard thin shell parameterization,

$$\mathbf{x}_i = \varphi(w_{i1}, w_{i2}) + w_{i3}\mathbf{n}_i(w_{i1}, w_{i2}) \,, \tag{1}$$

that expresses world-space coordinates $\mathbf{x}_i$ in terms of curvilinear coordinates $\mathbf{w}_i = (w_{i1}, w_{i2}, w_{i3})^T$ along the midsurface φ and its normal direction $\mathbf{n}(w_{i1}, w_{i2})$, respectively; see Fig. 3.

We use this curvilinear-space representation for both rest and deformed states. For the rest state, we define the parameterization such that substrate vertices have zero normal coordinates, i.e., $\bar{w}_{i3} = 0 \; \forall i$. The rest state map is simply the identity, i.e., $\bar{\varphi}(\cdot) = \text{id}(\cdot)$ and $\bar{\mathbf{x}}_i = \bar{\mathbf{w}}_i$. For the deformed state, we impose uniaxial states of curvature directly on the map (1). For example, the midsurface corresponding to cylindrical bending along the y-axis takes the form

$$\phi(w_{i1}, w_{i2}) = \left(-\frac{1}{\kappa}\sin(-\kappa w_{i1}), w_{i2}, -\frac{1}{\kappa}\cos(-\kappa w_{i1})\right)^T \,, \tag{2}$$

where κ is the macro-level curvature. This expression can be extended to allow for cylindrical bending in arbitrary directions through simple coordinate transformations; see App. A.

The essence of this *first-displace-then-map* approach is to enable unit cell nodes to adjust their curvilinear-space coordinates such that the midsurface transformation (2) maps them into the energetically optimal location (Fig. 3, *bottom*). For contrast, consider the *first-map-then-displace* alternative where unit cell nodes are endowed with world-space displacements. To enforce curvature conditions on world-space configurations, we must first estimate the macroscopic curvature from the deformed unit cell, then draw it towards the desired direction and magnitude. Using our representation, the curvature is given by construction and deviations from it can be measured solely in terms of normal displacements w_3. Our representation also facilitates the enforcement of periodicity conditions as we explain next.

Periodic Boundary Conditions. To ensure a macroscopically consistent state of deformation, the deformed unit cell must tile with itself without gaps and overlaps. The representation described above enables us to enforce these periodicity conditions conveniently in curvilinear space as

$$w^i_{k1} - w^j_{k1} = d^{ij}_1 \quad \text{and} \quad w^i_{k2} - w^j_{k2} = d^{ij}_2 \,, \tag{3}$$

$$w^i_{k3} = w^j_{k3} \,, \tag{4}$$

$$\mathbf{n}^i_f = \mathbf{n}^j_f \,. \tag{5}$$

The first condition asks that all pairs of corresponding vertices $(\mathbf{w}^i_k, \mathbf{w}^j_k)$ on opposite patch boundaries $(i, j) \in \{(1, 2), (3, 4)\}$ must

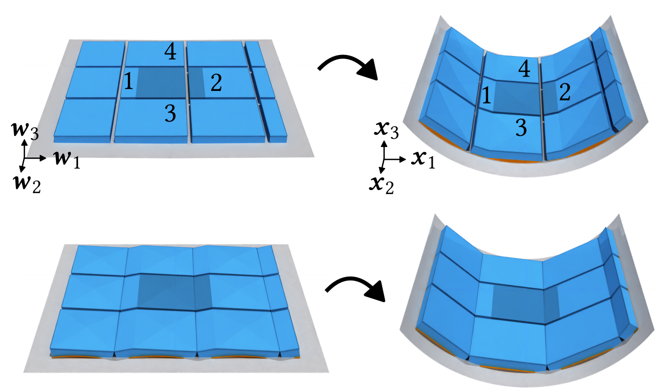

Fig. 3. Mapping from curvilinear space (left) to world-space (right) as described through Eq. (2). *Top*: a planar initial state leads to curved scales and high elastic energy in world-space. *Bottom*: curvilinear coordinates are optimized such as to minimize energy when mapped to world-space.

have the same in-plane displacements (d_1^{ij}, d_2^{ij}) (see Fig. 3, *top*). Condition (4) requires displacements in the normal direction to be identical. Finally, expression (5) requires that curvilinear-space normals $\mathbf{n}_i^f$ for corresponding boundary triangles $(\mathbf{w}_1^f, \mathbf{w}_2^f, \mathbf{w}_3^f)$ must match.

The unknown boundary displacements d_k^{ij} in (3) can be summarized as a symmetric linear transformation $\mathbf{F} \in \mathbb{R}^{2\times 2}$ that maps undeformed to deformed curvilinear-space directions as

$$(w_{k1}^j - w_{k1}^i, w_{k2}^j - w_{k2}^i)^T = \mathbf{F}(\bar{w}_{k1}^j - \bar{w}_{k1}^i, \bar{w}_{k2}^j - \bar{w}_{k2}^i)^T \ . \quad (6)$$

The symmetry of $\mathbf{F}$ ensures that no net rotations are applied to the unit cell during deformation.

Average Curvature. In addition to the above conditions, we must ensure that the deformed unit cell exhibits the desired state of curvature. With vanishing normal displacements, $w_{i3} = \bar{w}_{i3} = 0 \ \forall i$, the unit cell would smoothly track the midsurface, which has the desired curvature by construction. Due to the presence of stiff scales, however, the sheet cannot bend in a smooth fashion. Instead, the deformed sheet will assume an approximately piece-wise linear shape—regions of the substrate below scales will remain straight such that the remaining gaps will absorb all deformations. Since constant curvature states cannot be obtained, we ask that the target curvature should be matched in an average sense. Equivalently, deviations from the mid-surface must average out, i.e., $\int_\Omega w_3 d\Omega = 0$. In the discrete setting, this constraint becomes $\mathbf{e}_3^T\mathbf{M}\mathbf{w} = 0$, where $\mathbf{M}$ is the mass matrix of the substrate and $\mathbf{e}_3 = (0, 0, 1, \dots, 0, 0, 1)^T$.

Contact. To properly model large bending deformations of the unit cell, we must handle contact between the scales of the cell itself as well as with its immediate neighbors. To this end, we use the Incremental Potential Contact approach by Li et al. [2020] to construct C^2-continuous barrier functions for reliable contact handling. We collect all intra- and inter-cell contacts in a penalty term W_{contact} that is added to the potential energy of the unit cell.

Numerical Solution. For a given desired uniaxial curvature, we obtain the deformed configuration of the unit cell as the solution to the constrained optimization problem

$$\begin{aligned} \text{argmin}_{\mathbf{w},\mathbf{F}} \quad & W_{\text{substrate}} + W_{\text{scales}} + W_{\text{contact}} && (7) \\ \text{s.t.} \quad & (3), (4), (5), (6), && \\ \text{and} \quad & \mathbf{e}_3^T\mathbf{M}\mathbf{w} = 0 \ . && (8) \end{aligned}$$

We enforce the periodicity constraints (3—6) via variable substitution, whereas the curvature constraint (8) is handled using the Augmented Lagrangian method (ALM)—see, e.g., [Nocedal and Wright 2006]. More specifically, we define the objective function for the ith outer iteration as

$$\mathcal{L}(\lambda^i, \rho^i, \mathbf{w}^i) = -\lambda \boldsymbol{e}_3^T \boldsymbol{M}\boldsymbol{w}^i + \rho(\mathbf{e}_3^T \boldsymbol{M}\mathbf{w}^i)^2 \ , \quad (9)$$

where λ_i is a Lagrange multiplier and ρ_i is the constraint weight. We solve each ALM sub-problem by minimizing $\mathcal{L}$ with respect to $(\lambda^i, \mathbf{w}^i)$ using Newton's method with diagonal damping and update the Lagrange multiplier after each iteration. Since differentiating $\mathcal{L}$ results in a dense Hessian, we use the Sherman-Morrison formula to efficiently solve the corresponding linear systems.

3.3 Macro-Mechanical Model

To predict the behavior of scaled sheet materials on larger domains, we develop a macromechanical model that captures the principal characteristics in a computationally efficient way. In particular, we aim to capture anisotropy in bending elasticity, asymmetric stiffening beyond direction-dependent curvature limits, and strong resistance to bi-axial curvature. To account for these effects in a computationally efficient way, we opt for discrete shell elements based on a per-triangle discretization of the shape operator [Gingold et al. 2004]. These elements provide complete curvature information in any direction, which is required to fit the highly anisotropic behavior of our scaled sheet materials. We complement the bending elements with linear triangle finite elements for in-plane deformations combined with an orthotropic St. Venant-Kirchhoff material [Pérez et al. 2017].

Unidirectional Model. From the native-scale simulations, we observe that the curvature-energy relationship for any given bending direction exhibits two quasi-quadratic regimes before and after contact. We also note that the flexural modulus (i.e., the bending stiffness) of the post-contact regime is much larger compared to the pre-contact regime. These observations suggest a piece-wise quadratic energy model in which the bending moment $m(\kappa)$ is C^0-continuous with respect to the principal curvature κ,

$$m(\kappa) = \begin{cases} a\kappa & \kappa \leq \kappa_0 \\ a\kappa_0 + b(\kappa - \kappa_0) & \kappa > \kappa_0 \end{cases} , \quad (10)$$

where a and b are the stiffness coefficients for the pre-contact and post-contact regimes, respectively, and κ_0 is the curvature at which the material switches regimes. The directional bending energy $E_{\text{bending}}(\kappa)$ is then the integral of the moments $m(\kappa)$.

Polar Model. Due to the high anisotropy of scaled sheet materials, the parameters a, b and κ_0 depend on the direction of principal curvature. To obtain a homogenized energy model that describes the moment-curvature relation in any direction, we uniformly sample directions and curvature magnitudes from the native-scale simulation data. For each direction θ_i, we then find the corresponding $a(\theta_i)$, $b(\theta_i)$ by fitting the energy function $E(\kappa)$ using native-scale curvature and energy data. To obtain a directionally-continuous representation of these unidirectional curves, we fit circular harmonics functions of the form

$$\tilde{s}(\theta) = \sum_{k=0}^{n} c_k \cdot \cos(2k \cdot (\theta - d_k)) \ , \quad (11)$$

where n is the number of harmonics terms and c_k, d_k are free parameters that are determined such as to minimize the deviation from the unidirectional parameters in a least-squares sense. In this way, we obtain three functions $\tilde{a}(\theta)$, $\tilde{b}(\theta)$ and $\tilde{\kappa}_0(\theta)$ that enable us to evaluate the macromechanical bending energy for arbitrary directions and curvatures. We use $n = 3$ for $\tilde{\kappa}_0(\theta)$ and $\tilde{b}(\theta)$, and $n = 2$ for $\tilde{a}(\theta)$ due to the lower directional variation of the initial bending stiffness. The resulting fits for a selected scale pattern are shown in Fig. 4.

To evaluate the macromechanical energy for a given bending element, we must convert its curvature tensor $\boldsymbol{\kappa} = (\kappa_{xx}, \kappa_{yy}, \kappa_{xy})^T$

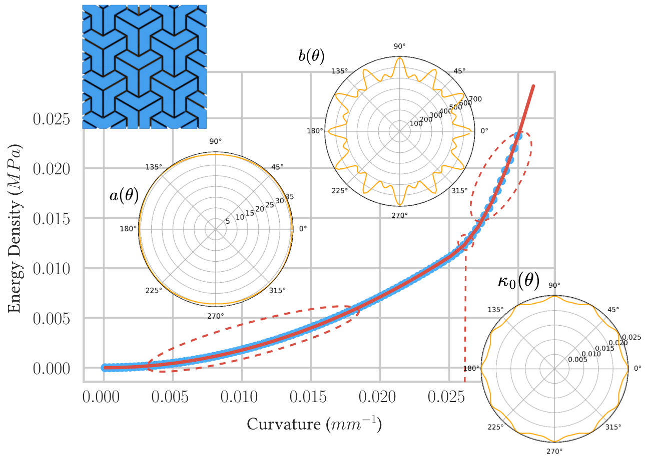

Fig. 4. Macro-scale parameters $a(\theta)$, $b(\theta)$ and contact curvature $\kappa_0(\theta)$ for a fitted circular harmonics (Eq. 11) are shown in *orange*. The blue dots in the energy density-curvature plot are sample points from the native scale simulation and the red line is the fitted piecewise-quadratic unidirectional energy density (Integral of Eq. 10) with slopes a and b and regime switch point k_0.

into principal curvatures κ_1, κ_2 and corresponding directions θ_1, θ_2. See App. B for details. The energy is then computed as

$$E_{\text{macro}}(\boldsymbol{\kappa}) = \sum_{j=1,2} E(\kappa_j(\boldsymbol{\kappa}); \tilde{a}(\theta_j(\boldsymbol{\kappa})), \tilde{b}(\theta_j(\boldsymbol{\kappa})), \tilde{\kappa}_0(\theta_j(\boldsymbol{\kappa}))) \; . \quad (12)$$

It is worth noting that we add contributions from both principal curvature directions to avoid discrete selection operations. This choice is justified by the strong resistance of scaled sheets to double curvature, which we enforce with an additional penalty term,

$$E_{\text{biaxial}} = \frac{1}{2} w_{\text{biaxial}} \det(\boldsymbol{\kappa})^2 \,, \quad (13)$$

where w_{biaxial} is the penalty weight.

Discussion. It should be noted that, even though our macromechanical model is based on piecewise quadratic energies, it is much more expressive than conventional anisotropic plate models: instead of fitting a single bending stiffness tensor that describes the moment-curvature response for all directions, we fit uni-directional parameters with a sampling interval of less than 2 degrees. This allows for larger variability with respect to direction, which is especially important for the contact curvature. As can be seen from Fig. 12, our macromechanical model is able to qualitatively reproduce the behavior of native-scale simulations. We further analyze the quantitative performance of our model in Sec. 4.

4 RESULTS

We used our method to characterize a diverse set of scale patterns from different isohedral tiling families. We analyze the mechanical behavior of a representative set of patterns and compare simulation results to experimental measurements. We furthermore evaluate our macro-mechanical model through comparisons to native-scale simulations. We start with a brief description of our manufacturing and measurement processes.

4.1 Manufacturing and Measuring Physical Prototypes

To generate 3D meshes for simulation and fabrication, we first create two-dimensional isohedral tessellations using the library *Tactile*[1]. The space of isohedral tilings consists of 93 families, each with up to 5 parameters that determine tile shape. From the 2D tessellation, we extract the tile polygons and the parallelogram corresponding to the periodic boundary. We then clip the polygons such as to obtain a gap of constant width between each scale. See also Fig. 2. The result of this operation is passed on to the *Gmsh* software in order to generate two periodic meshes, one for the substrate and one for the scales. Scale meshes are generated by extruding the resulting polygons from the previous step.

Fabrication. We follow the same process to generate printable scale meshes on rectangular domains of the desired size. The substrate is extruded in the normal direction to obtain a volumetric layer with given thickness. To ensure good adhesion between the scales and their substrate, an interlocking groove pattern was added at the based of each scale (see Fig. 5*d*). Finally, the scale mesh is cut and processed such as to fit different measurement devices. For omnidirectional curvature tests, we cut the mesh into a disc shape using boolean operations. For unidirectional force-displacement measurements, the mesh is cut into a rectangle and hinges are added on both sides. Rectangular and circular scale samples of 10cm length and 10cm radius, respectively, where fabricated using a Prusa $mk3s^+$ 3D printer equipped with a 0.4mm nozzle (Fig. 5*a*). The layer thickness was set to 0.1 mm, the number of perimeter tracks was set to 3 and gyroid infill was used. A 0.4mm thick substrate made of NinjaFlex TPU shore 85A was printed with 4mm tall PETG scales on top. This combination of materials exhibits relatively good adhesion while providing suitable stiffness properties.

For simulation, we used material parameters reported in the manufacturer's datasheet. For the substrate (TPU), we used a Young's modulus of 26MPa and 0.48 for the Poisson's ratio. For the scales (PETG), we used 2.02GPa for the Young's modulus and 0.35 for the Poisson's ratio.

Measurement Setups. We use two experimental setups to measure the mechanical behavior of our scaled sheets. The first one uses disc-shaped samples of 10cm radius mounted onto a mandrel rotating at a constant angular velocity of 4.5deg/s. A simple force probe is used to impose constant displacement at the boundary of the sample (see Fig. 6). A ball-bearing end-effector insures that the tool exhibits minimal friction force as the sample rotates. Readings from the force sensor are recorded continuously as the mandrel rotates, leading to a quasi-continuous force-displacement plot. We repeat measurements by doing 8 full rotations and plot the data for the last 6 ones.

Whereas the first setup measures a sample's response for a constant displacement in any direction, the second setup is used to characterize the nonlinearity of the material as a function of curvature for a given direction (see Figs. 10 and 11). We mount a rectangular

[1]See also https://isohedral.ca/software/tactile/

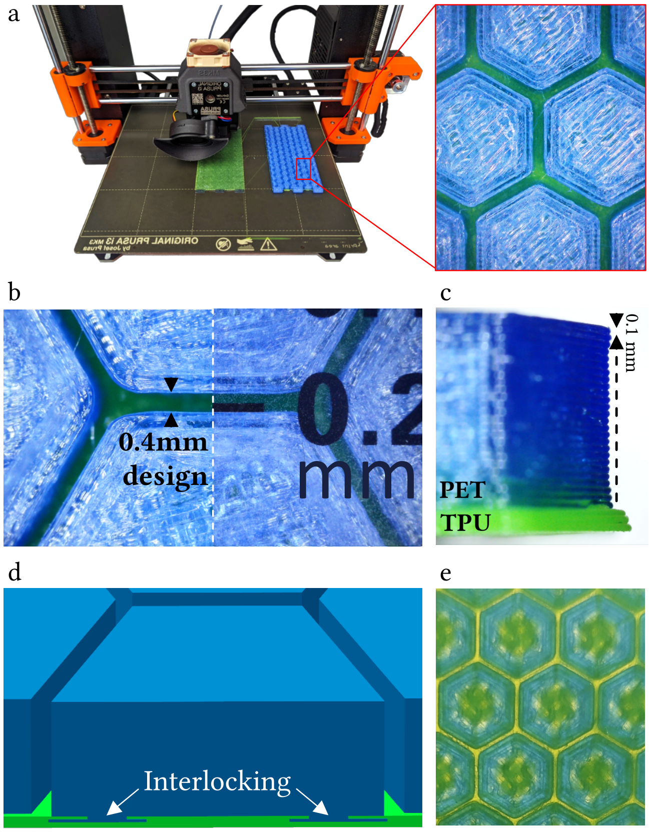

Fig. 5. We manufacture prototypes using 3D printing (*a*). The gap between scales (0.4mm) was controlled and straight edges with slightly rounded corners were observed (*b*). Layers of 0.1mm were used to print both the TPU substrate and the PET scales on top (*c*). An interlocking pattern was added to enhance adhesion between substrate and scales (*d*). Scales were filled using a gyroid pattern (*e*).

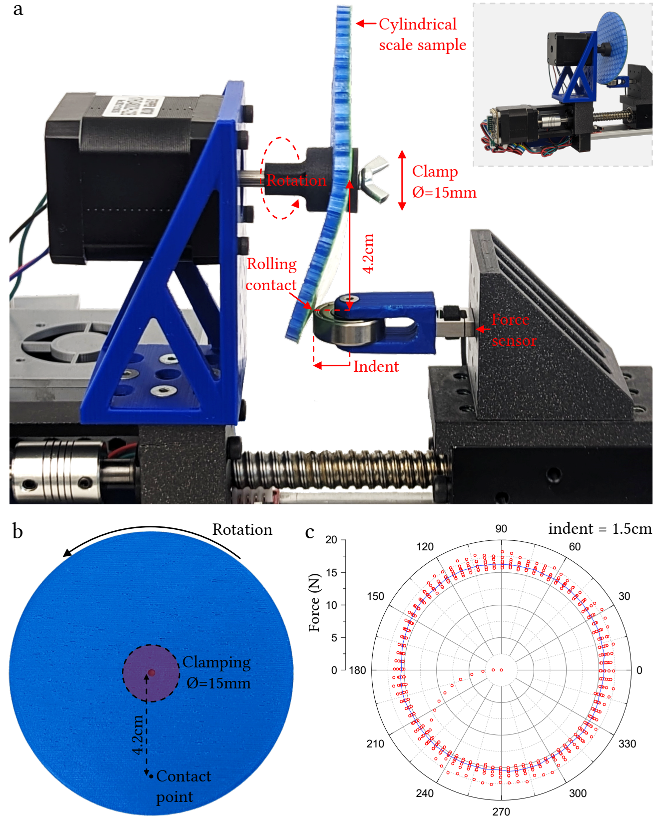

Fig. 6. Experimental setup for omnidirectional measurement of force-displacement response. *Top*: A disc-shaped sample is mounted onto a mandrel rotating at constant speed. A force probe imposes constant displacement at the boundary of the sample. *Bottom*: A 3D-printed solid disc is used for calibration. Force is recorded for 6 consecutive revolutions.

sample onto a linear stage using hinge joints. During the measurements, the distance between the hinge joints is decreased such as to impose an increasing curvature. The force required to maintain this curvature is measured using a load cell and the corresponding data is plotted.

4.2 Analysis and Exploration

We selected eight samples for our analysis to cover pattern symmetries from simple reflection to three-fold rotational, and scale shapes ranging from quasi-isotropic to anisotropic and from convex to concave shapes.

Contact-Induced Nonlinearity and Directional Variability. It can be seen from Figs. 7 and 8 that the selected patterns exhibit diverse and nonlinear moment-curvature responses. Even for small curvatures without contact, we observe large variability in bending stiffness within and across patterns, ranging from isotropic (Figs. 7*a* and 8*g*,*h*), to tetragonal (Fig. 7*b*), and to orthotropic (Figs. 7*c*,*d* and 8*e*,*f*). It is furthermore evident that for larger curvatures, contact between scales induces drastic changes. For all patterns, we observe a significant increase in bending stiffness in the contact regime. Furthermore, directional variation in the onset of contact leads to complex behavior. As can be seen from Figs. 7*b* and 8*f*, the directions of principal stiffness can change substantially due to contact. Moreover, the moment-curvature profiles generally exhibit more high-frequency features than at lower curvatures. One example illustrating this effect is the structure shown in Figs. 7*a* and 8*h*, which—although initially isotropic—exhibits distinct stiffness peaks at 60deg and 30deg angles, respectively, for larger curvatures. Finally, we also observe transitions between symmetry classes, e.g., from quasi-isotropic to tetragonal (Fig. 8*g*). From these results, we conclude that scaled sheet materials cover a wide range of complex moment-curvature profiles, and that contact between scales strongly influences this behavior.

To validate the results obtained through native-scale simulations, we performed experimental characterizations using the setup described in 4.1. It should be noted that the boundary conditions used in the experimental setup are different from the constant curvature

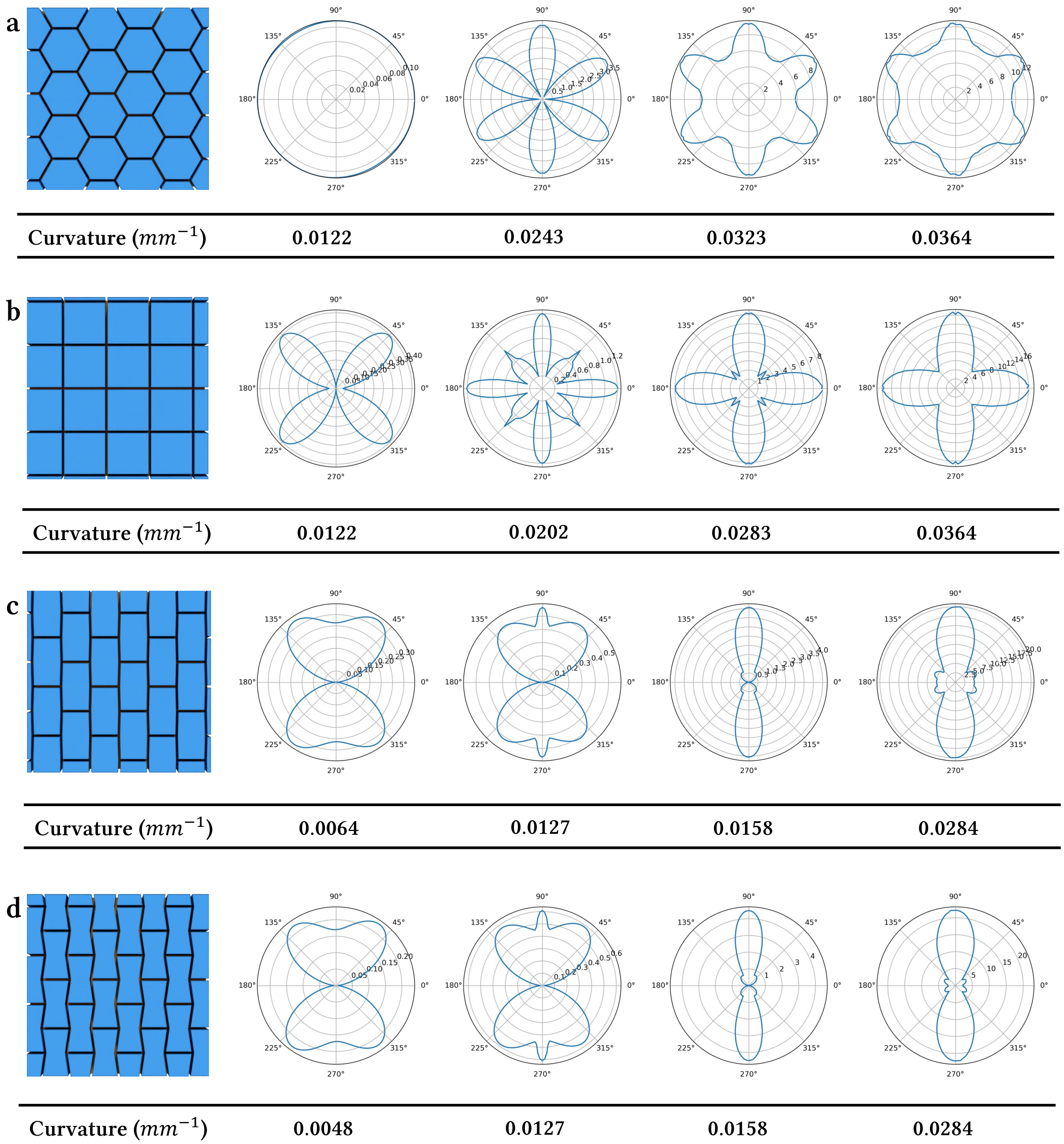

Fig. 7. Native-scale simulations, part 1. We show moment-curvature plots (columns *2-5*) for increasing curvature values on a set of patterns (column *1*).

conditions imposed in the corresponding simulations, such that meaningful comparisons can only be made with respect to qualitative behavior. These limitations notwithstanding , it can be seen from Fig. 9 that the experimental measurements for the post-contact regime are generally in good qualitative agreement with the behavior predicted in simulation. A slight exception to this rule is the three-fold symmetric structure shown in Fig. 9*h* for which measurements are not symmetric with respect to rotations by 180deg. This unusual behavior is explained by the way in which samples are mounted onto the mandrel, which immobilizes all scales adjacent to the sample's center. In combination with the fact that we only

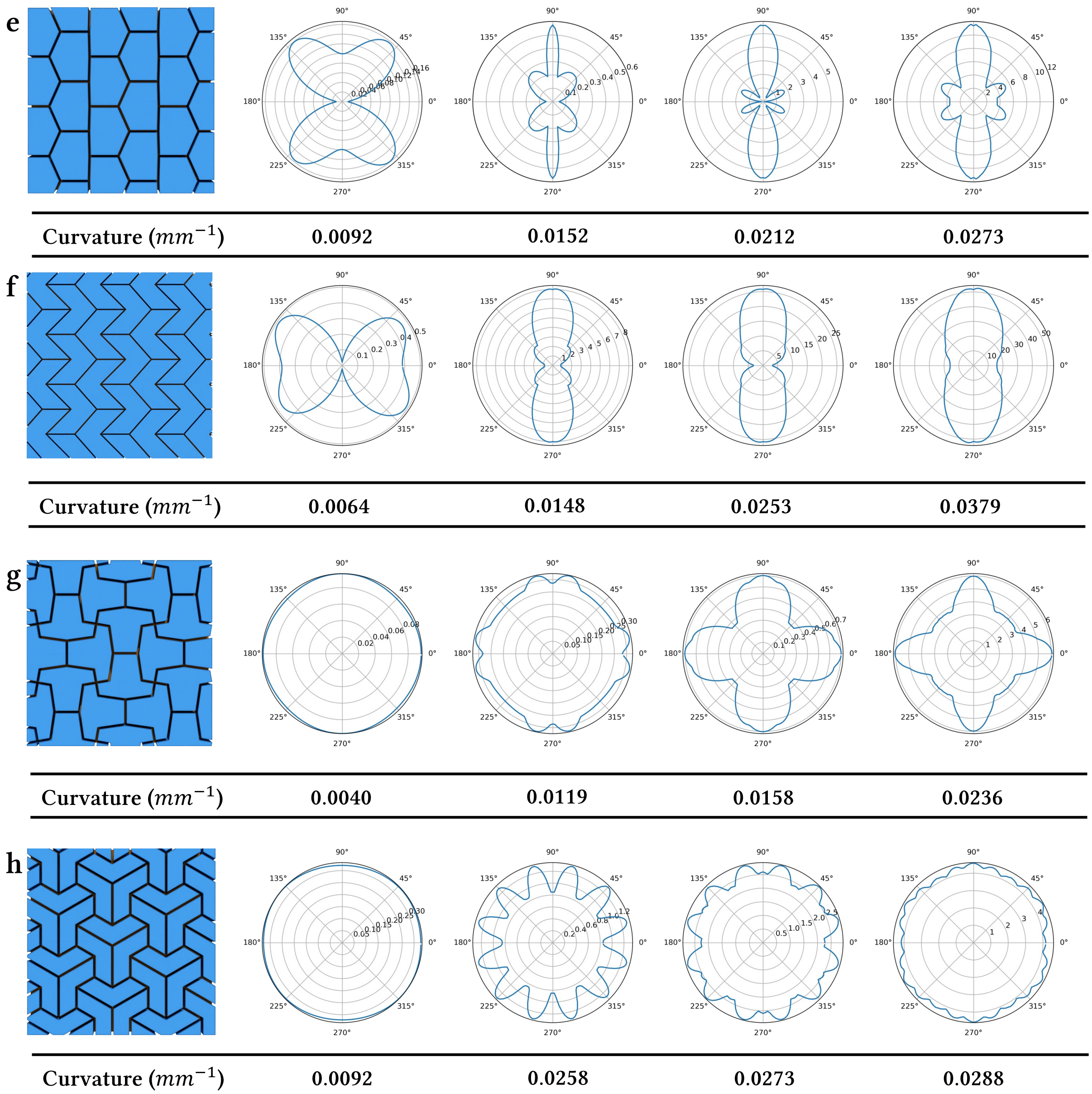

Fig. 8. Native-scale simulations, part 2. We show moment-curvature plots (columns *2-5*) for increasing curvature values on a set of patterns (column *1*).

impose curvature on one side at a time, this leads to slightly different free lengths from the sample's center to its boundary when applying 180deg rotations.

Influence of Pattern Symmetry. As shown by Schumacher et al. [2018] in the context of structured sheet materials, pattern symmetry translates into material symmetries. For example, a three-fold rotational symmetry implies an isotropic bending response for small curvatures. As can be seen from Figs. 7*a* and 8*h*, our three-fold symmetric scaled sheets obey this rule, each showing a circular moment-curvature profile. For larger curvatures, however, we observe lobe-shaped stiffness variations in our simulations whose number and frequency depend on both pattern and magnitude of curvature. The physical sample for the hexagonal pattern (Fig. 9*a*) confirms these predictions. Due to the aforementioned limitations in our measurement setup, these effects cannot be observed for the pattern shown in Fig. 9*h*. For patterns with four-fold rotational symmetry (Fig. 7*b*), we observe tetragonal behavior with equal stiffness in two orthogonal main directions as expected. Interestingly, the principal material axes rotate by 45deg for larger curvatures, but

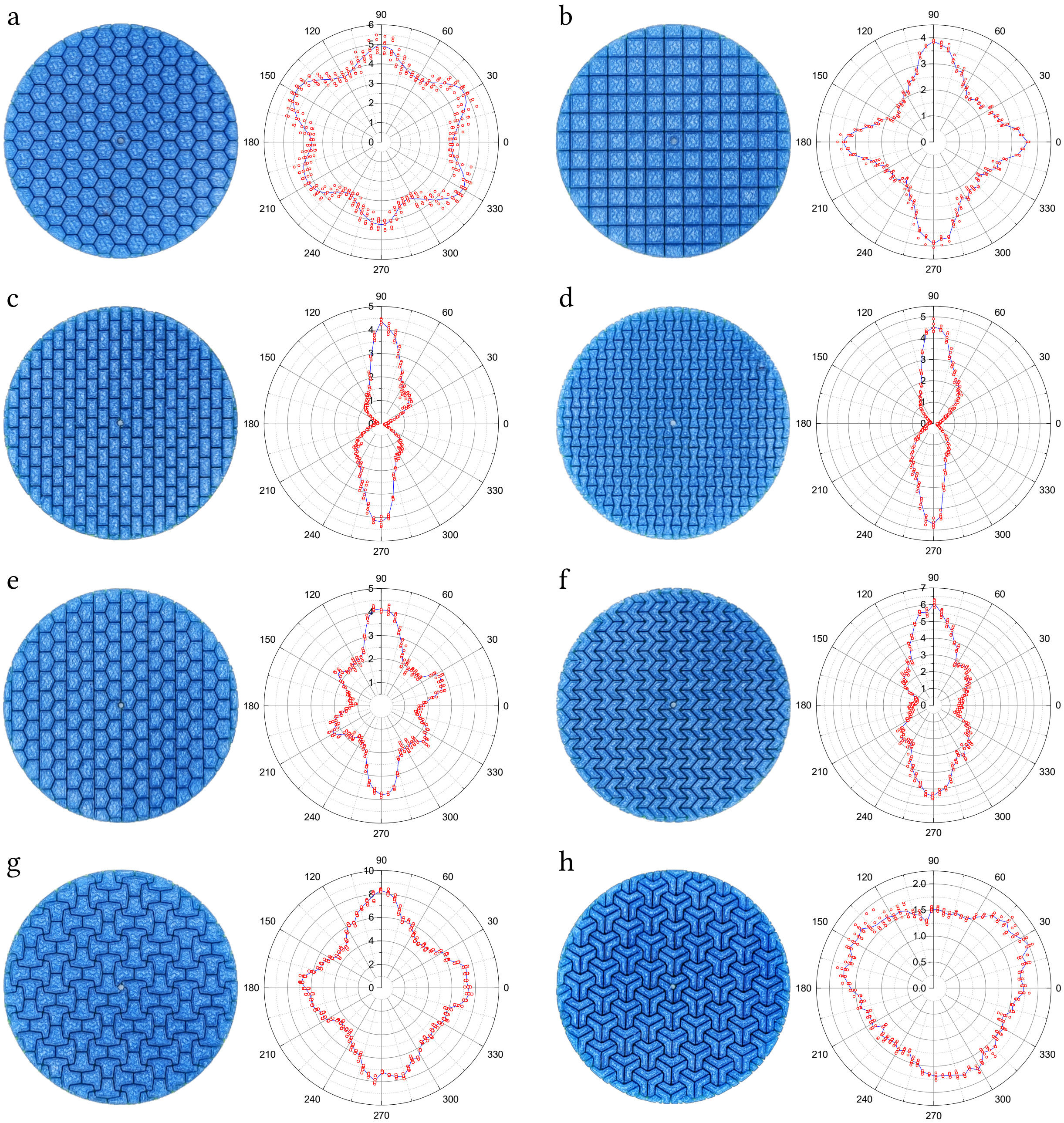

Fig. 9. Experimental characterization of scaled sheet materials using our omnidirectional bending setup (Fig. 6). We impose 1.5cm indentation at the boundary of each disc-shaped sample and plot the resulting force at equally-spaced sample locations for 6 full revolutions. Measured data is indicated in red, blue curves show averages of the 6 samples per direction.

the behavior remains tetragonal. Finally, patterns with one- or two-axis reflection symmetry (Figs. 7*c*,*d* and 8*e*,*f*,*g*) show orthotropic behavior for small curvatures in accordance with the linear theory. While the orthotropic behavior and principal directions remain unchanged, the minimum and maximum stiffness switch directions for the pattern shown in Fig. 8*f*).

Asymmetric Bending Response. In addition to omnidirectional measurements with constant displacement, we also perform uniaxial experiments to analyze the nonlinearity of the moment-curvature response (Figs. 10 and 11). One particular aspect that we seek to highlight in this context is the asymmetry in stiffness for positive and negative curvatures. For better clarity, we use the terms

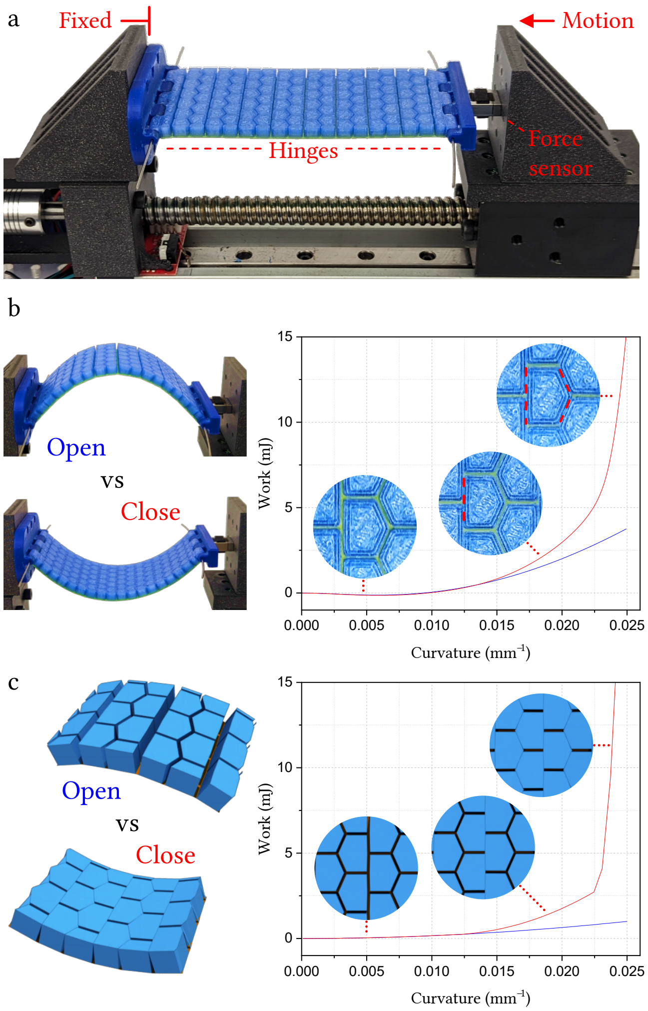

Fig. 10. Asymmetric bending resistance. (*a*) A linear stage is used to impose an increasing curvature while force is measured along the horizontal axis. (*b*) Opening and closing curvatures give rise to different force-displacement plots that start to diverge at the onset of contact. (*c*) Our native-scale simulation qualitatively reproduces this behavior.

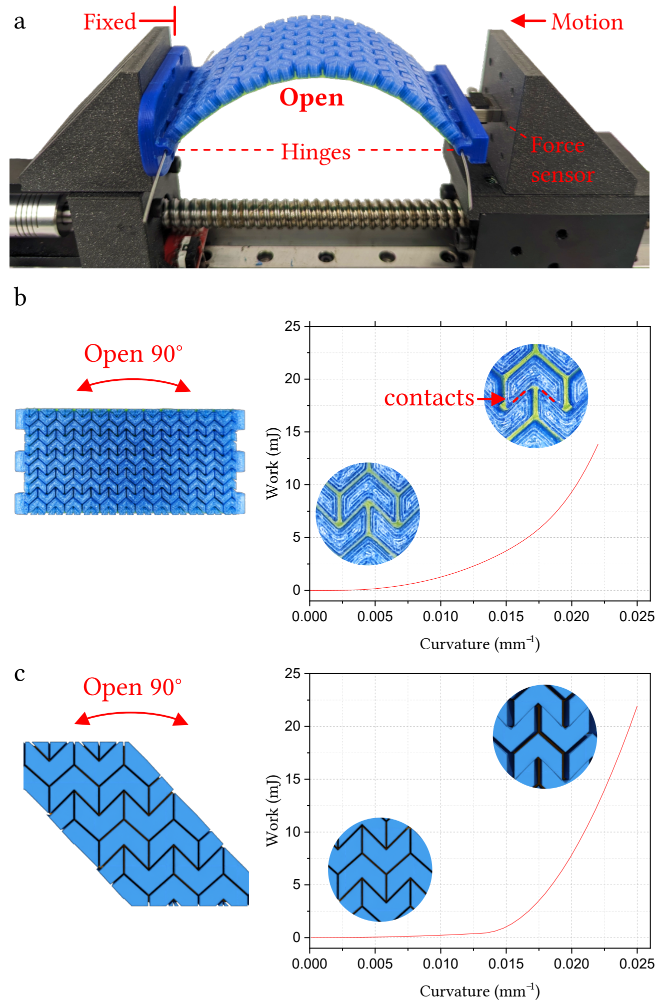

Fig. 11. Contact-induced stiffening for *opening* curvatures, using the same setup as in Fig. 10. (*b*) We record force-displacement behavior for opening curvatures of an arrow-like pattern, revealing contact induced stiffening (*red curve*) due to non-convex interlocking scales. (*c*) Our native-scale simulation reproduces the contact patterns and shows good qualitative agreement with experimental results.

opening and *closing* to indicate curvatures that tend to increase and reduce the gap between scales, respectively. For the pattern shown in Fig. 10, the stiffness for opening curvatures is very low and stays roughly constant beyond the initial range. For closing curvature, the behavior initially coincides with the opening direction. Once scales start to make contact, however, a significant stiffening is observed, leading to an overall bi-phasic moment-curvature relationship.

While closing curvatures always induce contact, depending on the pattern, opening curvatures can likewise lead to contact. The example shown in Fig. 11 illustrates this case on an arrow-like pattern. It can be seen from the force-displacement plots and the inset figures that bending in the given direction induces contact between scales and a corresponding stiffening. This effect can be explained by the concave shape of the scales, allowing them to interlock and resist opening curvatures. It is worth noting that this effect is highly direction-dependent and only occurs for non-convex scale shapes. As can be seen from Figs. 10 and 11, our native-scale simulation results successfully reproduce these experimental observations, showing qualitatively similar contact patterns among scales and a corresponding stiffening behavior.

Macro-mechanical Model. We evaluate the accuracy of our macromechanical model relative to the native-scale simulations by comparing moment-curvature profiles for different patterns. As can be seen from Fig. 12, the macro-scale model generally achieves good agreement with the reference data. For larger curvatures, the approximation is generally of high quality, whereas we observe larger deviations for some patterns (Fig. 12 *a,b*) at lower curvatures.

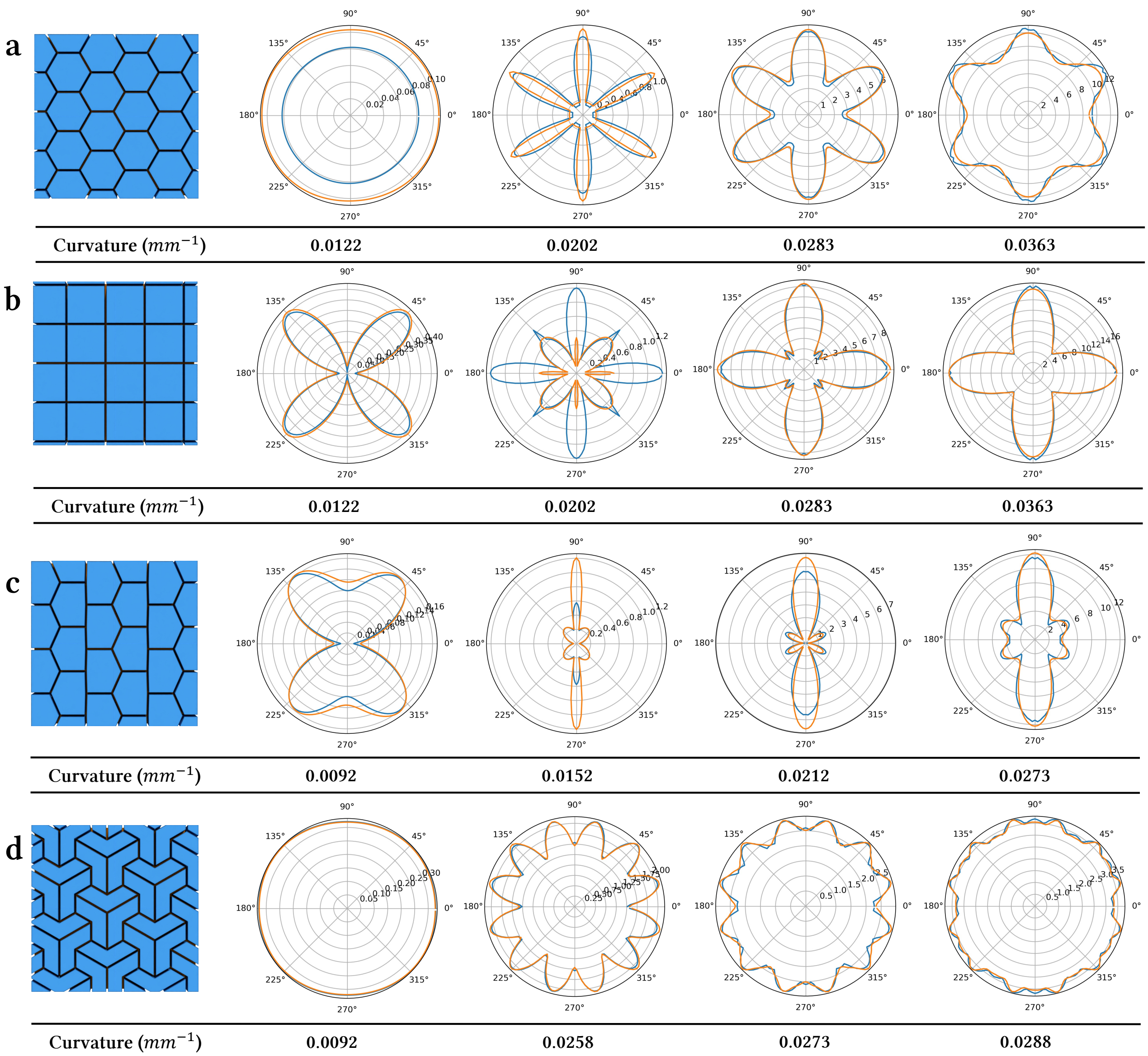

Fig. 12. Comparison between native-scale simulation results (*blue curves*) and our macro-mechanical model (*orange curves*) on four selected patterns (column *1*) and different curvatures (columns *2-5*).

This effect is arguably to the fact that our fitting approach minimizes absolute, not relative error, thus prioritizing larger curvatures which would otherwise induce larger errors (See supplemental material) . Nevertheless, considering the fact that the macro-scale model uses only 19 variables to represent the entire material behavior, the results are rather satisfying.

Synthesizing Scale Geometry for the Macro-mechanical Model. While our macro-mechanical model captures the bending behavior of the native-scale simulations, it does not provide scale-level geometry. To recover this information, we propose a simple method to synthesize scale geometry in a post-process to macromechanical simulations.

Starting from the triangle mesh used for macro-mechanical simulation, we generate a corresponding high-resolution scale mesh whose bottom faces are coplanar with the rest configuration of the simulation mesh. These scale mesh vertices are then converted to barycentric coordinates on the simulation mesh. For a given deformed simulation mesh, we estimate deformed scale positions through barycentric interpolation. For each scale, we compute the rigid transformation that best fits the estimated scale positions in two steps. First, we find optimal rotations using Procrustes analysis.

We then compute the optimal translation by minimizing per-vertex error in a least-squares sense. The result of this procedure can be seen in Figs. 13 and 14.

Large-Scale Simulation. Our macro-mechanical model is fitted to native-scale simulations that assume infinite patch sizes not found in real-world scenarios. We test the ability of our model to generalize to large structures with finite boundaries by comparing native-scale simulations of a 100mm×50mm rectangular sheet to shell simulations using our macro-mechanical model. We impose discrete curvatures ranging from 0mm^{-1} to 0.025mm^{-1}. As can be seen in Fig. 13, our model closely tracks the energetic response of the native-scale simulation for low curvatures and slightly overestimates it for larger curvatures.

Next, we evaluate the anisotropic response of our macro-mechanical model using the same rectangular sheet against the native-scale simulation with periodic boundary conditions. To this end, we rotate the scales in the sheet to align them with the direction of curvature of the native-scale simulation. Fig. 14 demonstrates that the two simulations agree very well despite the difference in boundary conditions.

Performance. To evaluate the performance of the macro-scale model, we compare computation times for the example shown in Fig. 13 for macro- and native-scale simulations. To properly model the geometry of the scales, the native-scale mesh requires 577,806 vertices and 575,477 faces while the macro-scale mesh needs only 2,746 vertices and 5,288 faces.

Both simulations run on a 24-core AMD 7960X machine with 64GB of memory. While the native-scale simulation takes 659,817ms to converge on average, our macro-scale model only requires 14,142ms, which corresponds to a 46-fold gain in performance. This difference is further increased for larger curvatures (see supplemental material).

5 CONCLUSIONS

We presented a new approach for computational modeling and mechanical characterization of scaled sheet materials. Our results indicate that our method is able to capture the complex mechanical effects induced by inter-scale contacts, including nonlinear stiffening, strong direction-dependence, and asymmetry in stiffness with respect to opening and closing curvatures. Our macromechanical model offers good approximation of the native-scale behavior at a fraction of the computational costs, thus opening the door to design

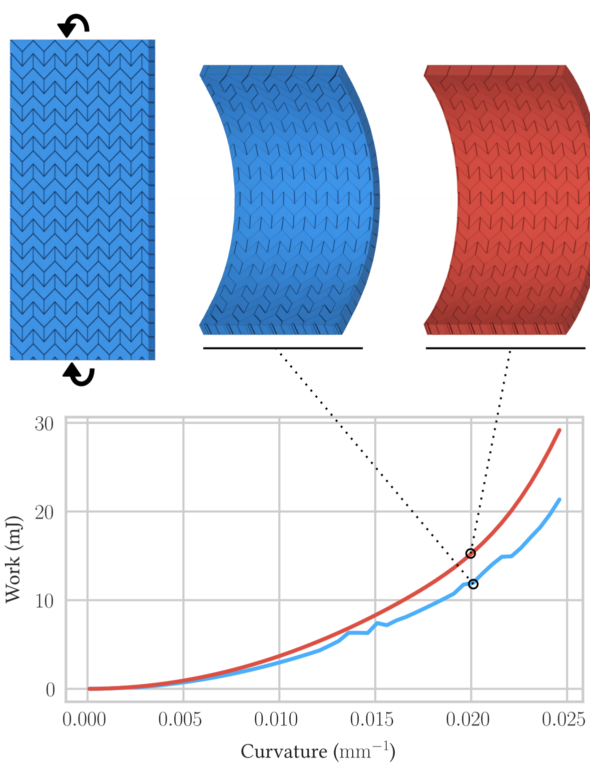

Fig. 13. Bending simulation of a 100mm×50mm rectangular sheet covered with arrow-shaped scales using the native-scale model (*blue*) compared against a shell simulation using the fitted macro-mechanical model (*red*).

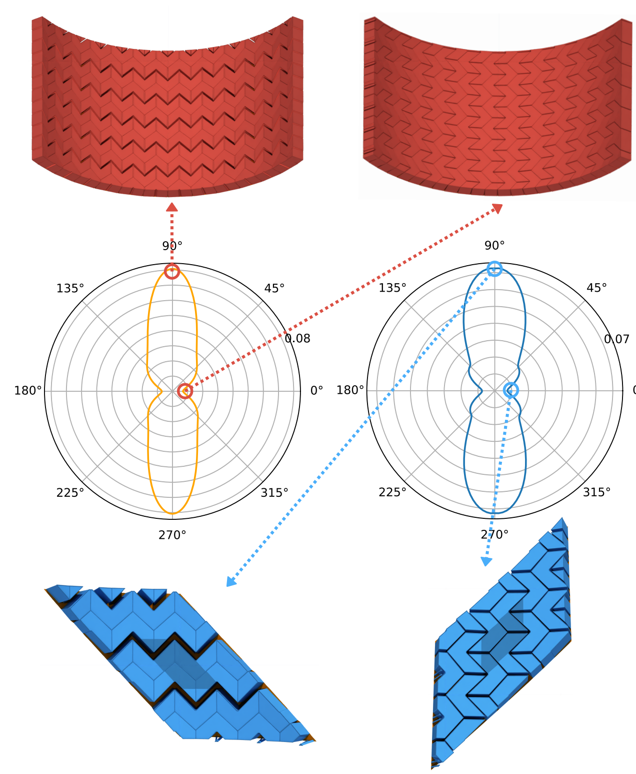

Fig. 14. Directional bending energy density for simulations using our macro-mechanical model for a 100mm×50mm rectangular sheet (*red*) compared against native-scale simulations with enforced periodic boundary conditions (*blue*). All simulations are run at a curvature of 0.02mm^{-1}.

tools that operate on large-scale simulations. An experimental analysis on 3D-printed samples confirms the qualitative predictions of our simulation models.

5.1 Limitations and Future Work

We have only considered periodic patterns from the isohedral tiling families, each of which is made from a single scale shape. While the space of patterns that can be generated in this way is large, tiling 3D surfaces with non-zero Gaussian curvature is impossible with a single tile shape. In the future, we would like to investigate approaches that allow for adaptive tiling with changing element shapes and topology, e.g., based on generalized Voronoi diagrams. Another possibility to create non-periodic scale patterns would be to use the star-shaped Voronoi diagrams of Martinez et al. [2019]. For the scales that we investigated in this work, interaction through contact only occurs at the scale boundaries. However, many animals possess overlapping scales that provide higher protection to puncturing. Exploring materials based on this concept, e.g., for protective sportswear is an exciting direction for future work. We designed our bi-phasic macromechanical model based on the assumption that scaled sheet materials exhibit a clear curvature threshold (per direction) at which contact between scales occurs. However, this assumption is not generally satisfied as some patterns may lead to contacts forming gradually with increasing curvature. While our method can still be applied to such materials, approximation errors will likely be more pronounced in these cases. Although our approach for generating scale-level geometry for macro-mechanical simulations often yields visually convincing results, it can induce intersections between synthesized scales. More advanced synthesis methods similar to [Sperl et al. 2021] might be able to avoid these problems. Finally, we would like to integrate scale simulation with inverse design algorithms such as to enable the creation of personalized protective gear and soft robotics skins that offer optimal flexibility and protection.

ACKNOWLEDGMENTS

We are grateful to the anonymous reviewers for their valuable comments. This work was supported by the European Research Council (ERC) under the European Union's Horizon 2020 research and innovation program (grant agreement No. 866480), and the Swiss National Science Foundation through SNF project grant 200021_200644.

REFERENCES

Moritz Bächer, Bernd Bickel, Doug L. James, and Hanspeter Pfister. 2012. Fabricating Articulated Characters from Skinned Meshes. *ACM Trans. Graph.* 31, 4, Article 47 (jul 2012), 9 pages. https://doi.org/10.1145/2185520.2185543

Alain Bensoussan, Jacques-Louis Lions, and George Papanicolaou. 1978. Studies in Mathematics and its Applications.

Katia Bertoldi, Vincenzo Vitelli, Johan Christensen, and Martin Van Hecke. 2017. Flexible mechanical metamaterials. *Nature Reviews Materials* 2, 11 (2017), 1–11.

Bernd Bickel, Moritz Bächer, Miguel A Otaduy, Hyunho Richard Lee, Hanspeter Pfister, Markus Gross, and Wojciech Matusik. 2010. Design and fabrication of materials with desired deformation behavior. *ACM Transactions on Graphics (TOG)* 29, 4 (2010), 1–10.

Duygu Ceylan, Wilmot Li, Niloy J Mitra, Maneesh Agrawala, and Mark Pauly. 2013. Designing and fabricating mechanical automata from mocap sequences. *ACM Transactions on Graphics (TOG)* 32, 6 (2013), 1–11.

Irene H. Chen, James H. Kiang, Victor Correa, Maria I. Lopez, Po Yu Chen, Joanna McKittrick, and Marc A. Meyers. 2011. Armadillo armor: Mechanical testing and micro-structural evaluation. *Journal of the Mechanical Behavior of Biomedical Materials* 4 (7 2011), 713–722. Issue 5. https://doi.org/10.1016/j.jmbbm.2010.12.013

Stelian Coros, Bernhard Thomaszewski, Gioacchino Noris, Shinjiro Sueda, Moira Forberg, Robert W. Sumner, Wojciech Matusik, and Bernd Bickel. 2013. Computational Design of Mechanical Characters. *ACM Trans. Graph.* 32, 4, Article 83 (jul 2013), 12 pages. https://doi.org/10.1145/2461912.2461953

Yotam Gingold, Adrian Secord, Han Jefferson, Eitan Grinspun, and Dennis Zorin. 2004. A Discrete Model for Inelastic Deformation of Thin Shells. In *Proc. of the ACM/Eurographics Symposium on Computer Animation (SCA) 2004 (Posters track).*

Eitan Grinspun, Yotam Gingold, Jason Reisman, and Denis Zorin. 2006. Computing discrete shape operators on general meshes. In *Computer Graphics Forum*, Vol. 25. Wiley Online Library, 547–556.

Ruslan Guseinov, Eder Miguel, and Bernd Bickel. 2017. CurveUps: Shaping Objects from Flat Plates with Tension-Actuated Curvature. *ACM Trans. Graph.* 36, 4, Article 64 (jul 2017), 12 pages. https://doi.org/10.1145/3072959.3073709

Craig S Kaplan and David H Salesin. 2000. Escherization. In *Proceedings of the 27th annual conference on Computer graphics and interactive techniques*. 499–510.

Lily Kharevych, Patrick Mullen, Houman Owhadi, and Mathieu Desbrun. 2009. Numerical coarsening of inhomogeneous elastic materials. *ACM Transactions on graphics (TOG)* 28, 3 (2009), 1–8.

Kurt Leimer and Przemyslaw Musialski. 2020. Reduced-Order Simulation of Flexible Meta-Materials. *Proceedings - SCF 2020: ACM Symposium on Computational Fabrication.* https://doi.org/10.1145/3424630.3425411

Samuel Lensgraf, Karim Itani, Yinan Zhang, Zezhou Sun, Yijia Wu, Alberto Quattrini Li, Bo Zhu, Emily Whiting, Weifu Wang, and Devin J. Balkcom. 2020. PuzzleFlex: kinematic motion of chains with loose joints. In *2020 IEEE International Conference on Robotics and Automation, ICRA 2020, Paris, France, May 31 - August 31, 2020.* IEEE, 6730–6737. https://doi.org/10.1109/ICRA40945.2020.9196854

Minchen Li, Zachary Ferguson, Teseo Schneider, Timothy R Langlois, Denis Zorin, Daniele Panozzo, Chenfanfu Jiang, and Danny M Kaufman. 2020. Incremental potential contact: intersection-and inversion-free, large-deformation dynamics. *ACM Trans. Graph.* 39, 4 (2020), 49.

Yue Li, Stelian Coros, and Bernhard Thomaszewski. 2023. Neural Metamaterial Networks for Nonlinear Material Design. *ACM Trans. Graph.* 42, 6, Article 186 (dec 2023), 13 pages. https://doi.org/10.1145/3618325

Lin Lu, Andrei Sharf, Haisen Zhao, Yuan Wei, Qingnan Fan, Xuelin Chen, Yann Savoye, Changhe Tu, Daniel Cohen-Or, and Baoquan Chen. 2014. Build-to-Last: Strength to Weight 3D Printed Objects. *ACM Trans. Graph.* 33, 4, Article 97 (jul 2014), 10 pages. https://doi.org/10.1145/2601097.2601168

Jonàs Martínez, Jérémie Dumas, and Sylvain Lefebvre. 2016. Procedural voronoi foams for additive manufacturing. *ACM Transactions on Graphics (TOG)* 35, 4 (2016), 1–12.

Jonàs Martínez, Mélina Skouras, Christian Schumacher, Samuel Hornus, Sylvain Lefebvre, and Bernhard Thomaszewski. 2019. Star-shaped metrics for mechanical metamaterial design. *ACM Transactions on Graphics (TOG)* 38, 4 (2019), 1–13.

Jonàs Martínez, Haichuan Song, Jérémie Dumas, and Sylvain Lefebvre. 2017. Orthotropic k-nearest foams for additive manufacturing. *ACM Transactions on Graphics (TOG)* 36, 4 (2017), 1–12.

Roberto Martini, Yanis Balit, and Francois Barthelat. 2017. A comparative study of bio-inspired protective scales using 3D printing and mechanical testing. *Acta Biomaterialia* 55 (6 2017), 360–372. https://doi.org/10.1016/j.actbio.2017.03.025

Juan Montes, Yinwei Du, Ronan Hinchet, Stelian Coros, and Bernhard Thomaszewski. 2023. Differentiable Stripe Patterns for Inverse Design of Structured Surfaces. *ACM Transactions on Graphics (TOG)* (2023).

Jorge Nocedal and Stephen J. Wright. 2006. *Numerical Optimization* (2e ed.). Springer, New York, NY, USA.

Julian Panetta, Abtin Rahimian, and Denis Zorin. 2017. Worst-case stress relief for microstructures. *ACM Transactions on Graphics (TOG)* 36, 4 (2017), 1–16.

Julian Panetta, Qingnan Zhou, Luigi Malomo, Nico Pietroni, Paolo Cignoni, and Denis Zorin. 2015. Elastic textures for additive fabrication. *ACM Transactions on Graphics (TOG)* 34, 4 (2015), 1–12.

Jesús Pérez, Miguel A. Otaduy, and Bernhard Thomaszewski. 2017. Computational design and automated fabrication of kirchhoff-plateau surfaces. *ACM Trans. Graph.* 36, 4, Article 62 (jul 2017), 12 pages. https://doi.org/10.1145/3072959.3073695

Emmanuel Rodriguez, Georges-Pierre Bonneau, Stefanie Hahmann, and Mélina Skouras. 2022. Computational Design of Laser-Cut Bending-Active Structures. *Computer-Aided Design* 151 (2022), 103335. https://doi.org/10.1016/j.cad.2022.103335

Stephan Rudykh, Christine Ortiz, and Mary C. Boyce. 2015. Flexibility and protection by design: Imbricated hybrid microstructures of bio-inspired armor. *Soft Matter* 11 (4 2015), 2547–2554. Issue 13. https://doi.org/10.1039/C4SM02907K

Christian Schumacher, Bernd Bickel, Jan Rys, Steve Marschner, Chiara Daraio, and Markus Gross. 2015. Microstructures to control elasticity in 3D printing. *ACM Transactions on Graphics (Tog)* 34, 4 (2015), 1–13.

Christian Schumacher, Steve Marschner, Markus Gross, and Bernhard Thomaszewski. 2018. Mechanical characterization of structured sheet materials. *ACM Transactions on Graphics (TOG)* 37, 4 (2018), 1–15.

Ali Shafiei and Francois Barthelat. 2022. 3D mechanics of scaled membranes. *International Journal of Solids and Structures* 241 (4 2022). https://doi.org/10.1016/j.ijsolstr.2022.111498

Ali Shafiei, J. William Pro, Roberto Martini, and Francois Barthelat. 2021. The very hard and the very soft: Modeling bio-inspired scaled skins using the discrete element method. *Journal of the Mechanics and Physics of Solids* 146 (1 2021), 104176. https://doi.org/10.1016/J.JMPS.2020.104176

Mélina Skouras, Stelian Coros, Eitan Grinspun, and Bernhard Thomaszewski. 2015. Interactive Surface Design with Interlocking Elements. *ACM Trans. Graph.* 34, 6, Article 224 (nov 2015), 7 pages. https://doi.org/10.1145/2816795.2818128

Mélina Skouras, Bernhard Thomaszewski, Stelian Coros, Bernd Bickel, and Markus Gross. 2013. Computational design of actuated deformable characters. *ACM Transactions on Graphics (TOG)* 32, 4 (2013), 1–10.

Peng Song, Chi-Wing Fu, and Daniel Cohen-Or. 2012. Recursive Interlocking Puzzles. *ACM Trans. Graph.* 31, 6, Article 128 (nov 2012), 10 pages. https://doi.org/10.1145/2366145.2366147

Peng Song, Chi-Wing Fu, Yueming Jin, Hongfei Xu, Ligang Liu, Pheng-Ann Heng, and Daniel Cohen-Or. 2017. Reconfigurable Interlocking Furniture. *ACM Trans. Graph.* 36, 6, Article 174 (nov 2017), 14 pages. https://doi.org/10.1145/3130800.3130803

Georg Sperl, Rahul Narain, and Chris Wojtan. 2020. Homogenized yarn-level cloth. *ACM Trans. Graph.* 39, 4 (2020), 48.

Georg Sperl, Rahul Narain, and Chris Wojtan. 2021. Mechanics-Aware Deformation of Yarn Pattern Geometry. *ACM Trans. Graph.* 40, 4, Article 168 (jul 2021), 11 pages. https://doi.org/10.1145/3450626.3459816

Ondrej Stava, Juraj Vanek, Bedrich Benes, Nathan Carr, and Radomír Měch. 2012. Stress relief: improving structural strength of 3D printable objects. *ACM Transactions on Graphics (TOG)* 31, 4 (2012), 1–11.

Pengbin Tang, Stelian Coros, and Bernhard Thomaszewski. 2023. Beyond Chainmail: Computational Modeling of Discrete Interlocking Materials. *ACM Trans. Graph.* 42, 4, Article 84 (jul 2023), 12 pages. https://doi.org/10.1145/3592112

Bernhard Thomaszewski, Stelian Coros, Damien Gauge, Vittorio Megaro, Eitan Grinspun, and Markus Gross. 2014. Computational Design of Linkage-Based Characters. *ACM Trans. Graph.* 33, 4, Article 64 (jul 2014), 9 pages. https://doi.org/10.1145/2601097.2601143

Davi Colli Tozoni, Jérémie Dumas, Zhongshi Jiang, Julian Panetta, Daniele Panozzo, and Denis Zorin. 2020. A low-parametric rhombic microstructure family for irregular lattices. *ACM Transactions on Graphics (TOG)* 39, 4 (2020), 101–1.

Franck J. Vernerey, Kamtornkiat Musiket, and Francois Barthelat. 2014. Mechanics of fish skin: A computational approach for bio-inspired flexible composites. *International Journal of Solids and Structures* 51 (1 2014), 274–283. Issue 1. https://doi.org/10.1016/j.ijsolstr.2013.10.001

Ziqi Wang, Peng Song, Florin Isvoranu, and Mark Pauly. 2019. Design and Structural Optimization of Topological Interlocking Assemblies. *ACM Trans. Graph.* 38, 6, Article 193 (nov 2019), 13 pages. https://doi.org/10.1145/3355089.3356489

Ziqi Wang, Peng Song, and Mark Pauly. 2018. DESIA: A General Framework for Designing Interlocking Assemblies. *ACM Trans. Graph.* 37, 6, Article 191 (dec 2018), 14 pages. https://doi.org/10.1145/3272127.3275034

Shiqing Xin, Chi-Fu Lai, Chi-Wing Fu, Tien-Tsin Wong, Ying He, and Daniel Cohen-Or. 2011. Making Burr Puzzles from 3D Models. *ACM Trans. Graph.* 30, 4, Article 97 (jul 2011), 8 pages. https://doi.org/10.1145/2010324.1964992

Wen Yang, Irene H Chen, Bernd Gludovatz, Elizabeth A Zimmermann, Robert O Ritchie, Marc A Meyers, W Yang, I H Chen, M A Meyers, B Gludovatz, E A Zimmermann, and R O Ritchie. 2013. Natural Flexible Dermal Armor. *Advanced Materials* 25 (1 2013), 31–48. Issue 1. https://doi.org/10.1002/ADMA.201202713

Jiaxian Yao, Danny M. Kaufman, Yotam Gingold, and Maneesh Agrawala. 2017. Interactive Design and Stability Analysis of Decorative Joinery for Furniture. *ACM Trans. Graph.* 36, 2, Article 20 (mar 2017), 16 pages. https://doi.org/10.1145/3054740

Zhan Zhang, Christopher Brandt, Jean Jouve, Yue Wang, Tian Chen, Mark Pauly, and Julian Panetta. 2023. Computational Design of Flexible Planar Microstructures. *ACM Trans. Graph.* 42, 6, Article 185 (dec 2023), 16 pages. https://doi.org/10.1145/3618396

Qingnan Zhou, Julian Panetta, and Denis Zorin. 2013. Worst-case structural analysis. *ACM Trans. Graph.* 32, 4 (2013), 137–1.

Bo Zhu, Mélina Skouras, Desai Chen, and Wojciech Matusik. 2017. Two-Scale Topology Optimization with Microstructures. *ACM Trans. Graph.* 36, 4, Article 120b (jul 2017), 16 pages. https://doi.org/10.1145/3072959.3095815

Lifeng Zhu, Weiwei Xu, John Snyder, Yang Liu, Guoping Wang, and Baining Guo. 2012. Motion-guided mechanical toy modeling. *ACM Transactions on Graphics (TOG)* 31, 6 (2012), 1–10.

A CYLINDRICAL BENDING IN ARBITRARY DIRECTIONS

We use the following transformations to compute mid-surfaces for uni-axial bending in arbitrary directions:

$$(w_1^r, w_2^r) = \boldsymbol{R}_{2\mathrm{D}}^T (w_1, w_2)^T \tag{14}$$

$$\varphi(w_1, w_2) = \boldsymbol{R}_{3\mathrm{D}} \left(-\frac{1}{\kappa} \sin(-\kappa w_1^r), w_2^r, -\frac{1}{\kappa} \cos(-\kappa w_1^r) \right)^T, \tag{15}$$

where $\boldsymbol{R}_{2\mathrm{D}}$ and $\boldsymbol{R}_{3\mathrm{D}}$ are rotation matrices defined with respect to the direction of bending $\alpha = [0, \pi)$ as

$$\boldsymbol{R}_{2\mathrm{D}} = \begin{pmatrix} \cos(\alpha) & -\sin(\alpha) \\ \sin(\alpha) & \cos(\alpha) \end{pmatrix}, \text{ and } \boldsymbol{R}_{3\mathrm{D}} = \begin{pmatrix} \cos(\alpha) & -\sin(\alpha) & 0 \\ \sin(\alpha) & \cos(\alpha) & 0 \\ 0 & 0 & 1 \end{pmatrix}.$$

B PRINCIPAL CURVATURES AND DIRECTIONS

The analytical forms of the curvatures and directions can be obtained by computing the eigenvalues $\boldsymbol{v}$ and eigenvectors $\boldsymbol{e}_{1,2}$ of a 2×2 matrix $[\kappa_{xx}\ \kappa_{xy}; \kappa_{xy}\ \kappa_{yy}]$, where

$$\boldsymbol{\lambda} = \begin{bmatrix} \frac{\kappa_{yy}}{2} + \frac{\kappa_{xx}}{2} + \frac{\sqrt{\kappa_{xx}^2 - 2\kappa_{xx}\kappa_{yy} + \kappa_{yy}^2 + 4\kappa_{xy}^2}}{2} \\ \frac{\kappa_{yy}}{2} + \frac{\kappa_{xx}}{2} - \frac{\sqrt{\kappa_{xx}^2 - 2\kappa_{xx}\kappa_{yy} + \kappa_{yy}^2 + 4\kappa_{xy}^2}}{2} \end{bmatrix}, \tag{16}$$

$$\boldsymbol{e}_1 = \begin{bmatrix} \frac{\kappa_{xy}}{\frac{\kappa_{yy}}{2} - \frac{\kappa_{xx}}{2} + \frac{\sqrt{\kappa_{xx}^2 - 2\kappa_{xx}\kappa_{yy} + \kappa_{yy}^2 + 4\kappa_{xy}^2}}{2}} \\ 1 \end{bmatrix}, \tag{17}$$

$$\boldsymbol{e}_2 = \begin{bmatrix} \frac{\kappa_{xy}}{\frac{\kappa_{yy}}{2} - \frac{\kappa_{xx}}{2} - \frac{\sqrt{\kappa_{xx}^2 - 2\kappa_{xx}\kappa_{yy} + \kappa_{yy}^2 + 4\kappa_{xy}^2}}{2}} \\ 1 \end{bmatrix}. \tag{18}$$

The direction of the first principal curvature can be computed as the angle θ_1 between two vectors $\boldsymbol{v}_1 = \kappa_{xy}$ and $\boldsymbol{v}_2 = \frac{\kappa_{yy}}{2} - \frac{\kappa_{xx}}{2} + \frac{\sqrt{\kappa_{xx}^2 - 2\kappa_{xx}\kappa_{yy} + \kappa_{yy}^2 + 4\kappa_{xy}^2}}{2}$, which is computed as,

$$2 \tan \frac{\theta_1}{2} = \frac{2\boldsymbol{v}_1 \times \boldsymbol{v}_2}{\|\boldsymbol{v}_1\| \|\boldsymbol{v}_2\| + \boldsymbol{v}_1 \cdot \boldsymbol{v}_2}. \tag{19}$$

The direction of the second principal curvature θ_2 can be likewise computed. However, curvature eigenvectors are not well-defined for repeated eigenvalues. For instance, for a flat sheet we have $\kappa_{xx} = \kappa_{xy} = \kappa_{yy} = 0$. To avoid this problem, we slightly perturb the computed curvatures to be non-zero when initializing our simulation. Other repeated-eigenvalue cases are avoided by the Gaussian curvature penalization term (see Eq. 13).